

ANALYSIS OF GAS TURBINE RIM CAVITY INGESTION WITH  
 AXIAL PURGE FLOW INJECTION

Christopher W. Robak<sup>1</sup>, Amir Faghri<sup>2</sup>, Karen A. Thole<sup>3</sup>

<sup>1</sup>Pratt & Whitney, East Hartford, CT, USA

<sup>2</sup>Department of Mechanical Engineering, University of Connecticut, Storrs, CT, USA

<sup>3</sup>Department of Mechanical and Nuclear Engineering, The Pennsylvania State University, University Park, PA, USA

ABSTRACT

Turbine rim cavities require an adequate supply of cooling purge flow to prevent hot gas ingestion from overheating metal components beneath the gas path airfoils. Purge flow is typically introduced into rim cavities through a labyrinth seal at the inner diameter of the cavity, or through conduits in the metal walls of the rim cavity. This numerical study will focus on purge flow introduced through axial holes in the stationary side of a turbine realistic rim cavity. Three dimensional Unsteady Reynolds-average Navier-Stokes (URANS) CFD modeling is utilized to model of cavity sealing effectiveness as a function of axial purge flow rate. CFD modeling is compared with experimental data from the test turbine in the Steady Thermal Aero Research Turbine (START). Results show good agreement with experimental data, especially at lower purge flow rates. Analytical depictions of the flow field setup in the rim cavity are provided, explaining trends observed in experimental data. Differences in sealing effectiveness trends between the upper and lower portions of the rim cavity are predicted by CFD modeling, adding insight to ingestion phenomena in turbine realistic rim cavities with complex geometry and flow leakage paths.

NOMENCLATURE

$C_{ax}$	Axial Blade Chord
$C_d$	Loss Coefficient
MGP	Main Gas Path
$P_s$	Static Pressure
$P_t$	Total Pressure
$Re_\theta$	Rotational Reynolds Number, $Re_\theta = \frac{\rho\omega r^2}{\mu}$

$Re_{ax}$	Axial Reynold Number, $Re_{ax} = \frac{\rho u_{ax} c_{ax}}{\mu}$
RC	Rim Cavity
$RPMF$	Non-dimensional circumferential velocity
RS	Rim Seal
V	Velocity
b	Hub radius
c	CO <sub>2</sub> concentration
r	Radius
u	Velocity
w	Width
$\epsilon_c$	Sealing Effectiveness
$\Phi$	Non-dimensional purge flow rate
$\Phi_{ref}$	Min flow to achieve purged rim cavity
$\Theta$	Circumferential Position
$\omega$	Rotational Speed
$\mu$	Dynamic Viscosity

Subscripts and Abbreviations

CPL	Cover plate leak
LS	labyrinth seal
SL	Serration leak
ax	Axial direction
purge	vane purge holes
rad	Radial direction
s	Purge air CO <sub>2</sub> concentration
tan	Tangential direction
vane	Vane position normalized
$\infty$	Background air CO <sub>2</sub> concentration

## BACKGROUND

Research in the field of ingestion phenomena in a gas turbine rim cavity is an active subject, with a focus on increasing part life and engine efficiency through improved design. Interest is driven by the need to prevent hot combustion gases from entering the secondary flow circuits, while keeping parasitic purge air consumption to a minimum. Rim cavities are used as a buffer between the hot gas path and the interior of the engine, where parts cannot tolerate high temperature operation. A balance between keeping metal components cool to extend part life and purge air consumption must be considered in rim cavity design.

To prevent hot gas ingestion into rim cavities, purge air is typically introduced into the cavity through orifices on the non-rotating structure, and through a seal between the rotating and stationary components. Purge air acts to pressurize the rim cavity to levels higher than the local gas path pressure, causing net outflow. The amount of purge air required to eliminate ingestion in rim cavities is of importance because it represents an efficiency penalty for the engine. The source of the purge air is taken directly from a compressor bleed or combustor bypass, reducing the amount of air entering the combustor. Additionally, air mixed into the gas path from the rim cavity induces loss which reduces turbine efficiency. Therefore, rim cavity design focuses on preventing hot gas ingestion with minimal amount of rim cavity purge air. To accomplish this end, novel rim cavity geometric designs need to be developed to reduce purge flow while keeping metal temperatures within acceptable limits. Numerical models are an inexpensive method of down selecting design concepts, but need further validation on complex geometries.

This paper presents a numerical study of ingestion in an engine realistic rim cavity. A brief review of literature in numerical studies is given to establish this work as a unique contribution of the field of research. A single purge flow configuration is considered where air is introduced through a series of orifice holes on the non-rotating structure towards the inner diameter of the rim cavity. Modeling results will be compared with measurement data presents in Clark et al. [1] for validation. The flow field in the engine-realistic rim seal is investigated.

## LITERATURE REVIEW

Early research into ingestion physics in rim cavities identified two distinct mechanisms for its occurrence. Owen and Rogers [2] theorized that ingestion in rim cavities is caused by external pressure variations at the mouth of the rim cavity, and by internal recirculation caused by boundary layer formation on the rotating and stationary surfaces. Externally induced ingestion, further described experimentally by Sangan et al [3] is responsible for driving gas path air into the rim cavity. During engine operation, the pressure potential field

from the static vane interacts with blade potential field, causing local circumferential peaks in pressure at the mouth of the rim cavity. Although the internal rim cavity pressure is higher than the average gas path pressure, the local gas path pressure can be higher than the rim cavity pressure across parts of the circumference, causing an influx of flow from the gas path to the rim cavity. Non-uniform circumferential pressure at the mouth of rim cavities is such a major driver for ingestion that many reduced order modeling predictions of ingestion use it as a primary input [2].

A second mechanism for ingestion described by Owen and Rogers [2] is rotationally induced ingestion. Further experiments by Sangan et al. [4] document the effects of rotation on the level of recirculation of flow in rim cavities. It is determined that boundary layer formation on both the rotating and stationary wall of rim cavities plays a critical role in the development of the flow field. The formation of the boundary layer on the rotating wall acts to pump fluid in the radial outboard direction. As the air moves outward it requires air from the inner diameter of the cavity to replace it. If the purge flow into the cavity is not enough to suffice the boundary layer pumping of the rotating wall, fluid will be drawn down the static structure, enhancing ingested flow.

More recently, unsteady cavity vortices have been identified as a third mechanism for ingestion. Beard et al. [5] measured the presence of unsteady flow structures in turbine rim cavities with Kulite pressure probes. Unsteady flow structures have previously been identified in CFD as a mechanism for ingestion [6,7], but not directly measured in a rim cavity experiment with high frequency pressure measurements. The generation of these structures is not well understood, but is reported to be a function of rotational speed and purge flow rates in rim cavities. Theories about their formulation include Kelvin-Helmholtz instabilities that are generated from a shear layer that forms between the highly swirled flow exiting the vane, and the relatively un-swirled purge flow exiting the rim cavity [8]. CFD simulations have shown unsteadiness enhances mixing levels in the cavity, which can act to entrain gas path air.

Numerical studies in rim cavity ingestion research are focused in two techniques; simple one-dimensional models for ingestion and more complex CFD modeling. A simple, one dimensional model for ingestion in rim cavities is presented by Johnson et al. [9]. The model utilized the non-uniform pressure variation of the airfoils along with a loss coefficient term,  $C_d$ , for specific rim seal geometries to predict ingestion. The resulting ingestion predictions are accurate enough to make design choices for rim cavities as long as the cavity  $C_d$  is calibrated through experimental data. A similar technique is employed by Savov and Atkins [10], using geometry length scales and relative fluid velocities to predict ingestion levels over a range of published experimental data sets. Simple models can provide quick predictions of ingestion levels in rim cavities, but are not capable of depicting the flow fields, which provide insight for geometric design improvements. This type of modeling typically does not account for the variety of ways

purge flow can be delivered into rim cavities, along with various leakages into and out of the rim cavities in real engine configurations. For detailed rim cavity ingestion predictions, advanced modeling in the field of CFD is required.

Early CFD modeling of a gas path to rim cavity geometry was reported by Hills et al. [11]. A URANS model was developed to compare against rig data taken by Green and Turner at the University of Sussex rig. Results predicted ingestion to be strongly influenced by unsteadiness in the pressure field created by the rotating blade, supporting the external ingress theory presented by Owen [2]. Compared with the experimental data, this CFD model tended to under predict the level of static pressure distortion from the airfoil in the main gas path, and therefore under predicted the level of ingestion, especially at higher purge air flow rates.

More recent CFD studies of rim cavities feature increasing complex geometry and modeling techniques. Wang et al. [12] used a full wheel URANS CFD model to simulate a turbine rim seal rig at Arizona State University. The researchers found that the CFD model tended to over predict the level of ingestion measured in the rig. However, better matches to experimental data were generated when the CFD was run as a full wheel simulation. Pockets of air moving at different rotational speeds than the surrounding fluid were predicted in the full wheel CFD simulations. These local disturbances interact with the ingress of gas path air at the rim seal, influencing the amount of ingestion. Reduced sized sector models do not capture these flow features as accurately because their number is dependent on cavity purge flow rate and geometry, and is not always integral to the number of vanes and blades in the simulation. Mirzamoghadam et al. [13] continued running the Wang et al. CFD models for longer unsteady time periods and achieved an even better match to experimental data at low purge flow rates.

O'Mahoney et al. [14] took a different approach to rim cavity CFD modeling with the use of large eddy simulation (LES) instead of URANS which most researchers have used to date. LES modeling was compared with URANS modeling and experimental data collected on a turbine rig with rotational Reynolds numbers up to  $2.2 \times 10^6$ . In contrast to Wang et al. [12], a small sector size approach to modeling was used. In general, LES showed a closer match in sealing effectiveness, but both modeling techniques tended to over predict the level of ingestion measured in the rim cavity.

Most previous computational research in rim cavity ingestion makes use of rig data which features simple rim cavity geometries and flow conditions with  $Re_0 = 2.2 \times 10^6$  or less. It is assumed that the findings of this research will be applicable to real world gas turbine technology, which can reach  $Re_0 = 2 \times 10^7$  and above. This paper will present CFD simulations compared with experimental data taken at the Pennsylvania State Universities in the Steady Thermal Aero Research Turbine (PSU START) rig. Data was taken at rotational Reynolds numbers up to  $3.8 \times 10^6$  and blade inlet axial Reynolds numbers of  $1.4 \times 10^5$ , making it the closest data set to real turbine operation available. Validating RANS CFD

modeling at higher Reynolds number flows is of importance for making engine relevant predictions of ingestion.

Additionally, the START rig features an engine realistic flow system in the rim cavity, with multiple purge air sources. Previous CFD modeling of rim seal ingestion has typically been focused on single purge flow sources, all exiting to the gas path. Modeling presented in this research features multiple sources and sinks for purge flow air. In gas turbine rim cavities, a large sink for purge air includes flow that leaks beneath the blade platform, through gaps in adjacent blades into the gas path. This flow is not accounted for in most previous research, and it will be shown that the magnitude of these leakages have the ability to change the flow field in rim cavities.

Previous numerical research has focused on validating models with data from simple rim cavity rigs. The geometry in these rigs features axial and radial facing rim cavity walls with axisymmetric gas path end walls and standard airfoils [12-14]. The PSU START rig geometry includes three-dimensional rim cavity rotating and stationary walls, blade-vane end wall contouring on the inner diameter side of the gas path, and non-axisymmetric features like vane/blade mate-face gaps. To the author's knowledge, no published numerical research features geometry, flow sources, and Reynolds numbers close to what is presented in this paper.

## RIG FACILITY

An overview of the START rig and its capabilities is described by Barringer et al. [15]. The START rig is a research turbine capable of holding steady state vane inlet air flow of 12.5 lbm/s at 70 PSIA. Figure 1 shows a basic schematic of the rig and secondary flow system. The START rig consists of a 1.5 single stage turbine, with rim cavities forward and aft of the turbine disk. In this research, the forward rim cavity of the START rig schematic in Fig. 1 is of interest, as experimental data was not recorded in the aft cavity.

The START rig forward rim cavity features two sources of purge air that are controlled independently, shown in Figure 1. The first source of purge air, labeled as (1) in Fig. 1 passes through a set of axial holes beneath the first vane at location (a) into the rim cavity at location (c). A second purge air source, (2), passes through a pre-swirler at location (f), traverses outwards in radius, then through a stepped labyrinth seal at location (d), before entering the bottom of the rim cavity at location (c). In this research, the computational study will focus on the purge configuration utilizing air passing through axial orifices beneath the 1<sup>st</sup> vane, with purge from the pre-swirler disabled.

The START turbine features engine relevant turbine hardware, which introduces the possibility for additional leak paths not found in most turbine rigs. Three significant rim cavity leaks, other than the pre-swirl flow and vane axial orifice flow, are shown in Figure 1. The first leakage path of note originates from the fit between the turbine cover plate and disk, and will be referred to as the cover-plate snap leakage. This

leak, labeled as (3) in Figure 1, is driven by a pressure gradient between the rim cavity and the inner secondary flow cavity made up by the space between the cover-plate and disk. This additional leakage is added to the rim cavity beyond what the labyrinth seal and axial orifices provide.

The second leakage of note occurs between the blade and disk interface, labeled as leakage (4) in Figure 1. This is commonly referred to as the serration leakage, which flows out of the rim cavity and across the disk from location (c) to (g). This leakage arises from that fact that the blade-disk interface does not create a perfect seal, leaving axial leakage paths which connect the forward and aft rim cavities, (c) to (g) in Figure 1.

The third rim cavity leakage found in the START rig occurs between the top of the disk and the blade under platform, labeled as leakage (5) in Figure 1. Air from the rim cavity flows between the top of the disk and the underside of the blade, acting to cool both components. The air exits under the blade through segment gaps between blades and through a small leakage path to cavity (g) in Figure 1. This leakage is significant and can influence the level of ingestion in the rim cavity as the purge flow rate is varied, as will be shown in this publication.

On the stationary side of the rim cavity, a leakage path exists between the outer portion of the pre-swirler and the vane, flowing from location (e) to (b) in Figure 1. This leakage is commonly referred to as the chordal seal leak, as the vane mating surface is designed with an offset that forms a chord with the cylindrical pre-swirler rail, creating a line contact for sealing.

A second major stationary side leak path exists between vane set segment gaps. Purge air can flow radially outward from location (a) in Figure 1 to the main gas path through these discrete leak paths. Engine designs typically utilize feather seals, thin pieces of metal that sit between vane sets to reduce this leak.

Although leakage paths between vane segments and chordal seals exist in true engine architectures, these leakage paths are sealed off with RTV in the START rig for more precise control of the amount of purge flow entering the cavity from location a in Figure 1. These leakage paths are not modeled for true comparison with START rig data.

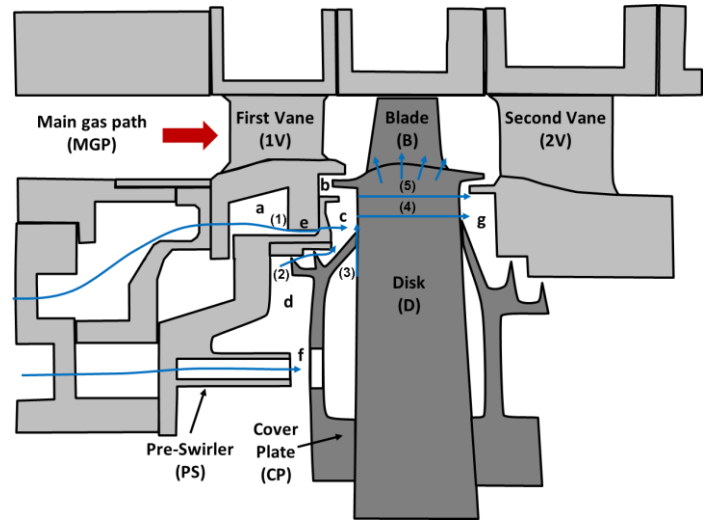


**Figure 1: START Rig Rim Cavity Leakage Paths, (1) through axial orifices, (2) through labyrinth seal, (3) through minidisk radial snap fit, (4) through blade to disk attachment, (5) through blade under platform**

Rig instrumentation includes static pressure and CO<sub>2</sub> measurement taps, the locations of which are shown in Figure 2. Temperature measurements of the purge and gas path air are taken with thermocouples. CO<sub>2</sub> concentration measurements are used to calculate the sealing effectiveness of the purge air, referred to as  $\epsilon_c$ . Sealing effectiveness is defined as the ratio of purge air to gas path air at any point in the rim cavity.

$$\epsilon_c = \frac{(c - c_\infty)}{(c_s - c_\infty)} \quad (1)$$

In Equation 1,  $c$  represents the measured concentration of CO<sub>2</sub> in the rim cavity,  $c_\infty$  is the background CO<sub>2</sub> concentration in the gas path, and  $c_s$  is the concentration of the CO<sub>2</sub> in the purge air. The START rig purge air is seeded with a known concentration of CO<sub>2</sub>, then a gas analyzer is used to determine the CO<sub>2</sub> concentration at sampling tap locations a, b, and c in Figure 2. As ingestion levels in the rim cavity change as a function of purge flow rate, the concentration of CO<sub>2</sub> measured at the sampling taps will vary, providing sealing effectiveness. Uncertainty in sealing effectiveness measurements is reported to be  $\pm 0.015$  to  $\pm 0.020$  effectiveness units [1]. The sealing effectiveness and static pressures measured in the START rig data set will serve to determine the accuracy of the CFD modeling presented in this paper relative to a real engine design cavity simulation.

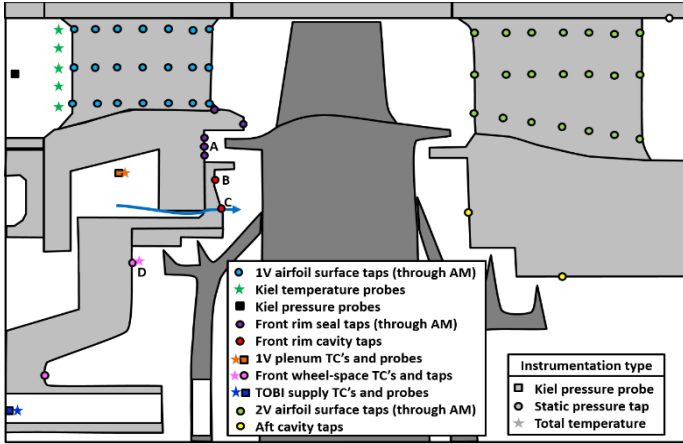


Figure 2: START Rig Instrumentation Locations

## COMPUTATIONAL METHODOLOGY

### Geometry and Model Setup

A 3D computational model of the START rig forward rim cavity is constructed from CAD geometry of the hardware. Figure 3 shows a schematic of the cavity dimensions as measured in the START rig. Geometric distances are normalized by the 1<sup>st</sup> vane hub radius,  $b$ , to provide relative distances between critical axial and radial rim cavity gaps. Purge flow enters the rim cavity, labeled as RC in Figure 3 at  $r/b = 0.941$ . The rim seal, labeled as RS in Figure 3, is defined from the pre-swirler discourager, located at  $r/b = 0.958$  to the inner diameter of the vane platform, at  $r/b = 0.990$ . Radii above  $r/b = 0.990$  are considered to be in the main gas path (MGP).

Axial and radial gapping of the CAD geometry is set to match measurements taken in the rig. Particular care is taken to accurately match the axial overlap of the vane trailing edge and the blade leading edge, as it has been shown to have an impact on the amount of ingested flow in rim cavities [9]. Axial and radial overlaps in the rim seal region of Figure 3 were measured with a combination of dial calipers and depth gauges. Reported measurement uncertainty was  $\pm 130 \mu\text{m}$  ( $\pm 0.005 \text{ in}$ ). Changes to the axial position of the rotor relative to the static structure during operation were controlled by the magnetic levitation bearing to within  $\pm 2.5 \mu\text{m}$  ( $\pm 0.0001 \text{ in}$ ). Radial dimensional changes were not measured directly but are expected to be within cold measurement uncertainty due to near room temperature rig operation and rotational speeds below 10,000 RPM.

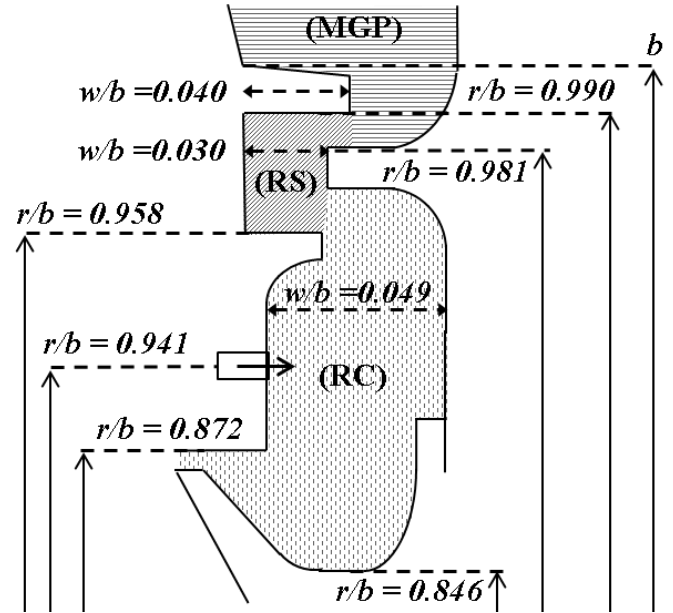


Figure 3: START Rig Rim Cavity Dimensions

The computational domain includes geometry for the partial span 1<sup>st</sup> vane and 1<sup>st</sup> blade airfoils in the START rig. The geometry beneath the 1<sup>st</sup> blade platform is modeled to capture the leakage path from the rim cavity, through the blade under platform, and out the blade damper seals and into the aft rim cavity, described in Figure 1. The 150 vane purge hole configuration reported by Clark et al. [1] is used for this study.

The CAD geometry was meshed in StarCCM+ version 11.06. A polyhedral element mesh is used with a wall function type viscous layer, yielding  $Y^+ \sim 30$ . Total mesh count for a 90° sector of the full wheel is approximately 22 million elements. Choice of a quarter wheel model is dictated by airfoils counts, with 90° being the minimum sector size without having to scale any of the airfoils from the true geometry shape. As will be discussed in the next section, grid independence studies were performed.

Meshed geometry is used to generate a solution in ANSYS Fluent commercial CFD software, version 17.1. The unsteady pressure-based Reynolds-Averaged Navier-Stokes solver is utilized. The K-Omega SST turbulence model is selected with the default Fluent settings and viscous dissipation enabled. The ideal gas equation of state is utilized, along with variable air properties as a function of temperature. Species equations are solved to track the concentration of CO<sub>2</sub> in the domain for comparison with rig data. Since the concentrations of CO<sub>2</sub> used to track ingestion are 1% or less in the rig, it is assumed that its effects on air properties are negligible. Therefore, species are tracked with either purge flow or gas path flow, both using the same properties as air. Thermal diffusion of the species is activated in the solver, although these effects are expected to be secondary with the turbulent flow regime of the gas path and rim cavity.

The SIMPLEC pressure-velocity coupling scheme is utilized [16], with 2<sup>nd</sup> order spatial discretization on momentum, density, species, and energy. The PRESTO! discretization [17] is utilized for pressure, and the turbulence equations are solved with 1<sup>st</sup> order discretization. Under-relaxation factors for the finalized solution are set to the Fluent default values. The time domain is solved with the first order implicate formulation, with 20 iterations per time step. Time step size is varied from coarse to fine, running a coarse time step to clear initial transient startup behavior in the solution for 5 wheel revolutions. A smaller time step is applied and run for an additional 3 wheel revolutions, with a domain time averaging of the last wheel revolution. The number of time steps per blade passing for the final time step size is in excess of 30 to capture the interactions between the vane and blade pressure potential fields.

The simulation is run in the parallel computing environment on 192 cores. The coarse time step completes one full wheel revolution in approximately 9.5 hours, the fine time step takes 48 hours, for a total run time of approximately 8 days. Solution convergence is tracked through a series of domain internal monitors of temperature, pressure, and CO<sub>2</sub> concentration with time step. Solutions are said to be converged when monitor averaged variables are changing less than 5% between full wheel revolutions.

## Boundary Conditions

The boundary conditions for the START rig CFD simulations originate from rig measurements at the turbine design condition. The gas path inlet and outlet boundary conditions are matched to that of the rig based on measured total pressure and temperature measurements upstream of the 1<sup>st</sup> vane, and static pressure measurements downstream of the 2<sup>nd</sup> vane. Turbine operation conditions include purge to main gas path density ratios between 1.1 and 1.3, a blade inlet relative Mach number of 0.2, a rotational Reynolds number of  $3.8 \times 10^6$ , and an axial Reynolds number of  $1.4 \times 10^5$  [1]. Turbine operating condition is held constant as purge flow is varied in the rim cavity.

Rim cavity purge hole boundary conditions are set to mass flow rates measured during START rig testing. Several rig internal flows including, the cover plate snap leak, labyrinth seal leak, and serration leak, are approximated in the model using an effective area and pressure ratio to derive a mass flow rate. The effective areas and pressure ratios across these three leakages are determined via a network flow model of the START rig. The network flow modeling utilizes correlations from historic engine and rig data to determine effective areas of the serration and cover plate-snap leaks. The labyrinth seal clearance is known from START rig measurements and is designed not to contact during operation. The network model uses a correlation with the measured seal clearance to approximate an effective area.

Flow through the blade under-platform cavity is resolved by the CFD solver. The leakage areas between blades

and into the aft rim cavity (see figure 1, location g) are set by the physical geometries in the START rig, allowing the flow rate to float with external boundary conditions applied to the overall model. Since the pressure ratio between the blade under platform and gas path is nearly constant across the range of purge flow rates tested in the START rig, the blade under platform cavity flow is expected to be constant.

Purge flow rates are non-dimensionalized as a function of the total flow rate required to seal the rim cavity to a sealing effectiveness greater than  $\epsilon_c > 0.99$ , as measured with rig data. This reference flow rate is defined as  $\Phi_{ref}$ , and mass flow boundary conditions are set as  $\Phi$ . Purge flow rates through the axial orifices are varied from  $\Phi_{purge} = 0.21$  to  $\Phi_{purge} = 0.80$ . In this study, the only source of rim cavity purge is through axial holes at location (e) in Figure 1. The orifice purge flow enters the rim cavity in the axially normal direction.

Although purge flow enters the rim cavity without circumferential velocity, the rotating walls of the disk-blade side of the rim cavity impose shear on the fluid. Rotation of the rim cavity air as a result of the rotating wall shear forces can be non-dimensionalized with the wall speed, presented in equation 2.

$$RPMF = \frac{V_{tan}}{2 * \pi * r * \omega} \quad (2)$$

The cover-plate snap leakage flow rate into the cavity is nearly constant with purge flow and contributes less than 5% of the total rim cavity purge flow at high flow conditions. The cover-plate snap leakage flow is assumed to enter the cavity at *RPMF* of 1.

Like the cover-plate flow, the serration leakage, diagramed in Figure 1, remains nearly constant as purge flow is increased. The serration leakage, defined by location 4 in Figure 1, is modeled as a constant mass flow extraction at the radial location of the blade-disk interface in the rim cavity. At low purge flow rates, the serration leakage can extract up to 50% of the purge flow introduced to the rim cavity. As purge flow level is increased, the serration leak reduces as a percentage of the overall flow purging the rim cavity.

Because the pre-swirl flow is disabled for experiments modeled in this work, flow is drawn backwards across the labyrinth seal out of the rim cavity to feed leakage paths across the disk of the START rig. During normal engine operation, the labyrinth seal would be a source of purge air to the rim cavity, however during these experiments the seal acts to draw a small amount of air towards the inner diameter of the rig. The flow rate is set by the measured pressure ratio across the seal, along with knowledge of the seal running clearance during operation.

A summary of the rim cavity boundary conditions can be found in table 1. Thermal boundary conditions are set to measured air temperatures, approximately 70°F. Turbulence boundary conditions follow Fluent recommended conditions, medium intensity and length scale 1/6 of the inlet hydraulic diameter.

**Table 1: Rim Cavity Boundary Conditions for CFD**

Vane Purge Flow ( $\Phi_{\text{purge}}/\Phi_{\text{min}}$ )	Labyrinth Seal Flow ( $\Phi_{\text{LS}}/\Phi_{\text{min}}$ )	Cover Plate Snap Leak ( $\Phi_{\text{CPL}}/\Phi_{\text{min}}$ )	Serration Leak ( $\Phi_{\text{SL}}/\Phi_{\text{min}}$ )
0.11	-0.08	0.03	-0.06
0.24	-0.07	0.01	-0.06
0.42	-0.06	0.01	-0.06
0.62	-0.09	0.04	-0.06
0.80	-0.11	0.04	-0.05

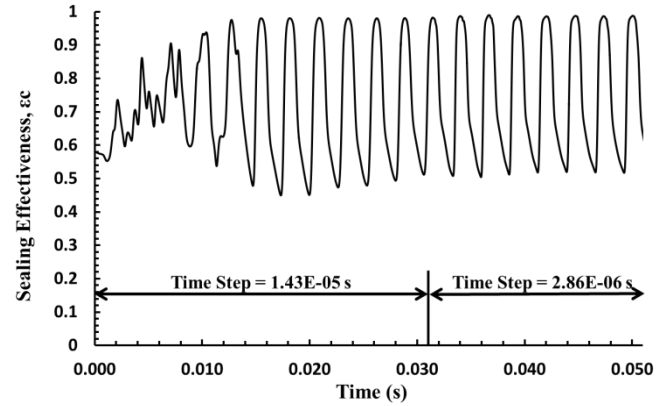
### Grid Independence Study

To determine whether the CFD model utilized in this study is grid independent, a second grid is generated with twice the mesh density and converged. The steady state solution of the two grid densities is compared on the 1<sup>st</sup> vane at 50% span in Table 2. Deviations in the static pressure field at the vane trailing edge are less than 0.2%, providing confidence that the medium grid mesh contains enough resolution to not influence the solution. To run multiple purge flow boundary conditions with limited computational resources, the medium density mesh is used for the CFD solutions presented in this study.

**Table 2: Grid Independence Study Statistics**

Grid	Total Cell Count	Normalized Vane TE Pressure at 50% Span (Ps/Pt,in)	Deviation
Medium	21.98 M	0.7243	--
Fine	39.04 M	0.7255	0.16%

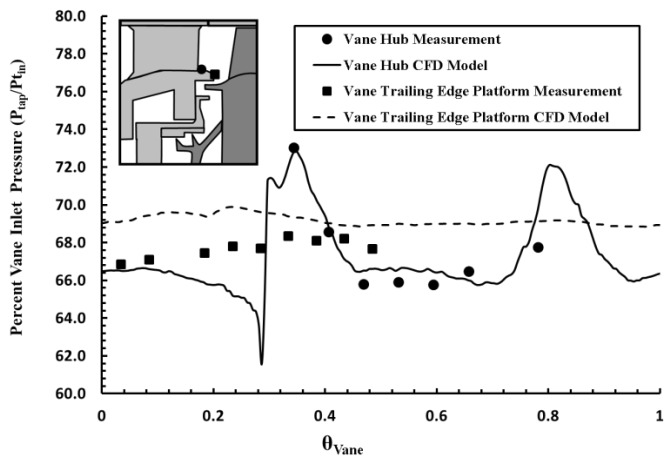
For the unsteady solution, several time step sizes are utilized to ensure a time step independent solution. All simulations are first converged to a steady state solution, then run unsteady with an initial time step of  $1.43 \times 10^{-5}$  seconds for 5 wheel revolutions. The initial coarse transient time step is performed to initiate the unsteady flow field in the rim cavity. Figure 4 shows a transient monitor point on the rim seal static wall (location A in Figure 2) of sealing effectiveness at a vane purge flow rate of  $\Phi_{\text{purge}}/\Phi_{\text{min}} = 0.21$ . Initially, the monitor records transient start up behavior of the solution through the first full revolution of the wheel. Once the initial transient start up is cleared, the monitor shows the rim seal falling into a cycle of increasing and decreasing sealing effectiveness, with a frequency of 400 Hz. This frequency is not integral to a hardware count, and at 2.5 engine orders is related to cavity instabilities. The frequency of this oscillation changes with purge flow rate and is not the same at all locations within the rim cavity geometry. This phenomenon has been documented in other rim cavity CFD modeling research [5]. However, the START rig did not have fast response Kulite pressure measurements to verify the existence of these instabilities.

**Figure 4: Sealing Effectiveness Transient Monitor on Rim Seal Static Structure for a Vane Purge Flow Rate of  $\Phi_{\text{purge}}/\Phi_{\text{min}} = 0.21$** 

After three complete revolutions, the time step is decreased by 5x to  $2.86 \times 10^{-6}$  s, then run for an additional 3 full wheel revolutions. The rim cavity monitor data in Figure 4 indicates little change in the solution. Peak to peak magnitude of the sealing effectiveness fluctuations does not change with the reduced time step. The frequency of the fluctuations also remains unchanged, and it is concluded that the solution does not show significant sensitivity to time step size.

### RESULTS

Rim cavity ingestion theory places high importance on vane-blade potential field interactions in the gas path of turbines to drive ingestion into the rim cavities [3]. Figure 5 shows static pressure distortions, non-dimensionalized by inlet pressure at the vane inner diameter hub and trailing edge platform, compared with rim cavity data with no purge flow activated. Pressure measurements are plotted as a function of non-dimensionalized  $\theta_{\text{vane}}$ , where  $\theta_{\text{vane}}$  is the circumferential position along a vane doublet. The comparison in Figure 5 is created from data and CFD modeling without purge flow to show the effects of the airfoils on the pressure field near the rim cavity entrance without purge flow influence.



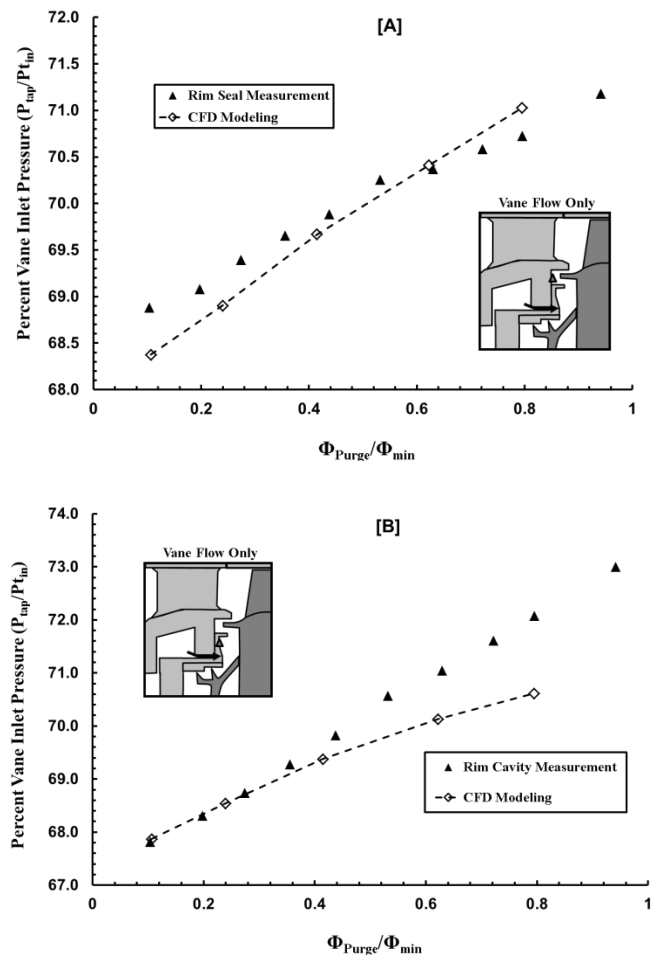
**Figure 5: Static Pressure Distortions at Vane Inner Diameter Hub and Trailing Edge; CFD Modeling Compared with Rig Data for Non-Purge Simulation**

Figure 5 shows that the CFD model is accurately capturing the static pressure distortion at the vane hub created by the potential field of the airfoil, a major driver for rim cavity ingestion. The peak to trough distortion is predicted to be 7% of the inlet total pressure. The double peak signature of the pressure field at the vane hub is indicative of the two vane airfoils contained in the vane pack. The discontinuity at  $\theta_{\text{vane}} = 0.29$  shows the effects of the mate-face gap between vane packs, which is explicitly modeled in the CFD simulation. On average, the model predicts static pressures within 1.5% of the experimental data for any given circumferential location.

At the vane trailing edge, CFD modeling predicts normalized static pressures on average 1.6% higher than data as indicated in Figure 5. Circumferential distortion of the static pressure field is attenuated from the hub distortion in both the CFD prediction and the rig data. Attenuation of pressure distortions from the gas path airfoils is expected to increase as radius in the rim cavity decreases, as demonstrated by pressure data presented in Clark et al [1]. Ingestion deep into the rim cavity is mainly driven by boundary layer effects and turbulent transport as the pressure field equalizes in the rim cavity.

Rim cavity static pressure comparisons between the CFD simulations and rig data are shown in Figures 6a and 6b as a function of non-dimensional purge flow at pressure tap locations in the rim seal and mid rim cavity. The CFD simulation, plotted with the dashed line, shows a linearly increasing cavity pressure as a function of purge flow rate. The trend agrees favorably with data in the rim seal location at non-dimensional cavity purge flow rates measured. A monotonic increase in cavity static pressure with purge flow rate is expected as increased in purge flow act to pressurize the rim cavity beyond the maximum static pressure distortions of the vane-blade potential fields in the gas path, reducing ingestion levels.

When rim seal pressure levels reach 71.2 % of the inlet total pressure, the cavity is measured to be fully purged ( $\Phi_{\text{purge}}/\Phi_{\text{min}} = 1$ ), and the static pressure in the rim seal is higher than all but the very peak of the distortion shown in Figure 5. Since the predicted CFD rim seal pressures are higher than data, the model is expected predict higher sealing effectiveness in this region, as the pressure potential for flow ingress is reduced to negligible amounts.



**Figure 6: Rim cavity pressure as a Function of Non-Dimensional Purge Flow, [A] Comparison at rim seal tap, [B], Comparison at rim cavity tap**

Within the rim cavity, START rig data indicates a sharper increase in static pressure with purge flow rate than the CFD model predicts, shown in Fig. 6b. At low purge conditions, static pressures compare favorably, but diverge as the purge flow is increased towards  $\Phi_{\text{purge}}/\Phi_{\text{min}} = 1$ . Differences in this region could be attributed to differences in swirl velocity driven by ingestion deep into the rim cavity. This would influence the level of swirling flow in the rim cavity, changing the vortex structure.

## Sealing Effectiveness Comparisons

Figure 7 compares sealing effectiveness measurements with CFD predictions in the rim seal region for vane purge flow rates up to  $\Phi_{\text{purge}}/\Phi_{\text{min}} = 0.8$ . Note the inset in Figure 7 shows the location within the rim seal region for the comparisons. In general, CFD over predicts sealing effectiveness by between 0.05 and 0.30 units, with the greatest divergence occurring at higher purge flow rates.

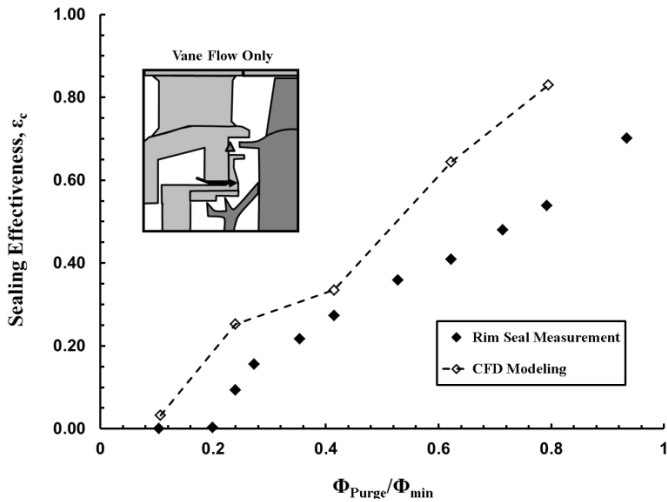


**Figure 7: Rim Seal Sealing Effectiveness as a Function of Non-Dimensional Purge Flow**

The CFD model is able to capture trends in sealing effectiveness observed in the data. At vane purge flow rates less than  $\Phi_{\text{purge}}/\Phi_{\text{min}} = 0.2$ , little to no sealing effectiveness is measured in the rim seal region. At these purge flow rates, the air being drawn across the blade under-platform cavity, represented in Figure 1, flow (5), is greater than the purge flow entering the vane holes. To maintain mass flow continuity in the rim cavity, air from the gas path must flow into the cavity to satisfy the blade under-platform flow. This type of forced ingestion is not typically seen in rigs, but does occur in real gas turbines due to imperfect seals between blades.

Once enough vane purge flow is introduced to satisfy all cavity leakage flows, the purge begins exiting the mouth of the rim cavity, represented by the increase in sealing effectiveness predicted and observed at purge flows higher than  $\Phi_{\text{purge}}/\Phi_{\text{min}} = 0.2$  as shown in Figure 7. As purge flow is increased, both CFD and experimental results show increasing sealing effectiveness, with CFD predicting higher increases than the measurements. The static pressure field prediction in Figure 6a is consistent with the higher effectiveness demonstrated in the rim seal at high purge flow rates.

Figures 8 and 9 provide data to CFD comparisons of effectiveness in the rim cavity upper and lower regions. Predictions agree with START measurements within 0.2 effectiveness units, with regions of relatively good match. In the upper rim cavity, shown in Fig 8, sealing effectiveness

begins to increase as vane purge flow is introduced to the cavity. The numerical simulation under predicts sealing effectiveness for  $\Phi_{\text{purge}}/\Phi_{\text{min}} < 0.2$ , and over predicts effectiveness for  $\Phi_{\text{purge}}/\Phi_{\text{min}} < 0.6$ .

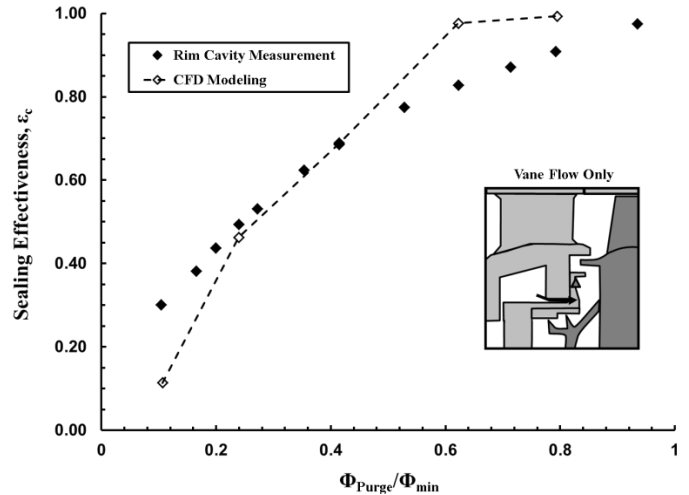


**Figure 8: Outer Rim Cavity Sealing Effectiveness as a Function of Non-Dimensional Purge Flow**

Sealing effectiveness at the purge hole radius, shown in Figure 9, matches trends between the CFD prediction and rig data. The CFD model under predicts sealing effectiveness by 0.20 units for  $\Phi_{\text{purge}}/\Phi_{\text{min}} = 0.5$ , and is in better agreement at higher vane purge flow rates, with a mostly purged cavity. Sealing effectiveness data indicates a small increase in sealing effectiveness for  $\Phi_{\text{purge}}/\Phi_{\text{min}} 0.1$  to 0.2, then a leveling in sealing effectiveness until  $\Phi_{\text{purge}}/\Phi_{\text{min}} = 0.5$ . This behavior is also predicted with the CFD model, although with lower absolute levels of ingestion. At purge levels higher than  $\Phi_{\text{purge}}/\Phi_{\text{min}} = 0.5$ , both CFD and data show an increase in sealing effectiveness towards unity, meaning a completely purged cavity at the measurement radial location.

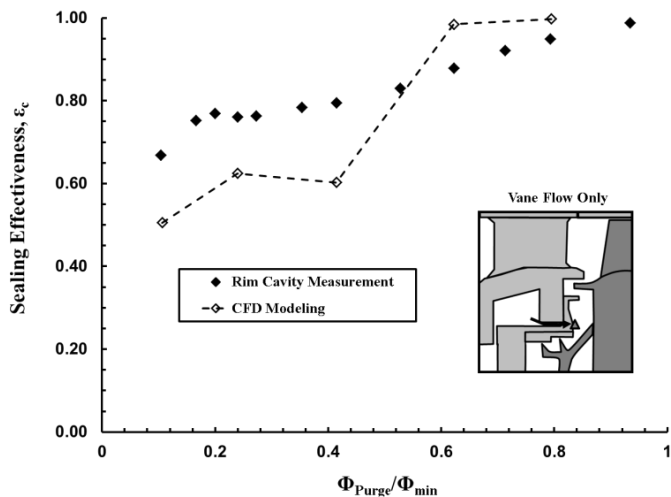


**Figure 9: Inner Rim Cavity Sealing Effectiveness as a Function of Non-Dimensional Purge Flow**

## DISCUSSION

Trends in sealing effectiveness at different measurement locations in the rim cavity have different patterns than reduced order modeling presented in previous research is able to predict [10]. The computational modeling of engine realistic rim cavities can give insight into trends in sealing effectiveness observed in rig data sets. Figures 10-12 show time averaged sealing effectiveness with superimposed fluid streamlines at a rim cavity cross-section, radial hole plane, and axial plane through the rim seal and lower rim cavity. Dashed lines on the depiction of the purge flow rate  $\Phi_{\text{purge}}/\Phi_{\text{min}} = 0.62$  in Figures 10-12 provide the relative position of the axial, radial, and cross-sectional planes to each other.

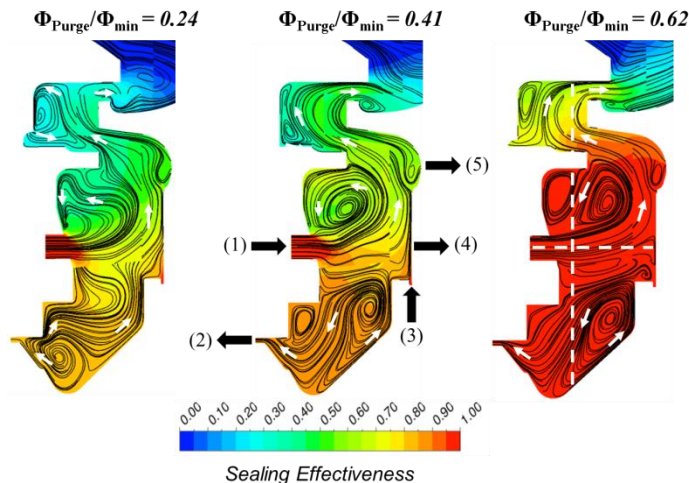


**Figure 10: Sealing Effectiveness with Cavity Streamlines as a Function of Purge Flow**

The CFD predictions show a complex flow structure in the rim cavity that is flow dependent. In general, the rim cavity is split into two different recirculation regions by the vane purge holes shown in Figure 10. Arrows provide the direction of these recirculation cells. Above the purge holes, flow recirculates in the pocket created by the pre-swirler static structure above the vane purge holes. Below the vane purge location, a secondary recirculation occurs as flow is pulled down towards the labyrinth seal. These two recirculation patterns remain relatively stable as the level of purge flow is increased in the rim cavity.

As flow makes its way from the rim cavity to the rim seal, as defined by Figure 3, it is forced to pass through a gap created with the blade wing and the upper portion of the pre-swirler geometry. This flow purging the rim seal area creates a recirculation region in the rim seal. As purge flow is increased, the recirculation cell is reduced and flow leaves the rim cavity with increasingly strong axial velocity.

The regions of circulation predicted by CFD can help to explain trends observed in the experimental data. Rim seal measurements in Figure 7 show sealing effectiveness does not begin to increase until  $\Phi_{\text{purge}}/\Phi_{\text{min}} = 0.2$ . This is explained by the blade under platform, serration, and labyrinth seal flow reducing the amount of purge that reaches the rim seal location. The reduced flow has low axial momentum so that the purge air is found to follow the rotating structure due to boundary layer pumping. This is observed for  $\Phi_{\text{purge}}/\Phi_{\text{min}} = 0.24$  and  $\Phi_{\text{purge}}/\Phi_{\text{min}} = 0.41$  in Figure 10 as lower sealing effectiveness predicted near the static structure where rig data is being measured. As  $\Phi_{\text{purge}}/\Phi_{\text{min}}$  is increased to levels greater than 0.62, higher concentrations of purge air are able to reach the static structure. This is also observed in the data set, with a slope change in sealing effectiveness beginning around  $\Phi_{\text{purge}}/\Phi_{\text{min}} = 0.65$  as shown in Figures 7-9.

Leakage flow across the blade under platform only increases slightly as the purge flow from the vane into the rim cavity is increased and rim cavity pressure gradually rises. For  $\Phi_{\text{purge}}/\Phi_{\text{min}} = 0.2$ , enough purge flow is supplied to the rim cavity to satisfy the blade under platform leak, and purge flow is detected in the rim seal. The CFD predictions shows purge flow making it into the rim seal at  $\Phi_{\text{purge}}/\Phi_{\text{min}} = 0.1$ . Leakage from the blade under platform to the gas path is calculated internal to the CFD domain using an estimated leakage area between blade segments. Errors in estimated areas compared with actual leakage areas can lead to discrepancies in predicted flows compared with actual flows. Local concentration effectiveness is sensitive to changes in local leakage flow, as demonstrated by the differences between CFD modeling and experimental data as to when purge flow is detected in the rim seal region. It follows that modeling of turbine realistic rim cavities need to incorporate all possible leakage sources and sinks to increase accuracy in the numerical predictions of ingestion.

At the rim cavity measurement location in Figure 8, the shape of the sealing effectiveness curve follows the shape suggested by the reduced order modeling of the cavity [1]. The

trend in sealing effectiveness for this location is well predicted by the numerical model. The dominant recirculation above the vane purge hole causes strong mixing to occur in this region of the rim cavity, especially above  $\Phi_{\text{purge}}/\Phi_{\text{min}} = 0.24$ . This mixing reduces purge flow concentration axial gradients in the rim cavity, making the trend in sealing effectiveness more continuous than in other locations in the rim cavity. The unique geometry of the static structure at this location may be acting to promote the recirculation cell shown in Figure 10 directly outboard of the purge hole radius.

At the purge hole radius, a different trend in sealing effectiveness is both predicted by the CFD and observed in the rig. This difference in sealing effectiveness is directly related to the radial location of the purge holes. In Figure 9, a nearly constant sealing effectiveness is observed for  $\Phi_{\text{purge}}/\Phi_{\text{min}}$  less than 0.4. Figure 11 shows time averaged sealing effectiveness on an axial plane bisecting the rim cavity with superimposed streamlines at varying  $\Phi_{\text{purge}}/\Phi_{\text{min}}$ . A strong axial gradient of purge air is predicted at the purge hole radius, with air above the purge holes having a greater concentration of gas path ingested air than below the purge hole radius. The location of the purge holes is evident by a localized increase in the sealing effectiveness near the jets created by the discrete holes. Jets created by the vane purge holes are shown in Figure 12 at varying  $\Phi_{\text{purge}}/\Phi_{\text{min}}$ .

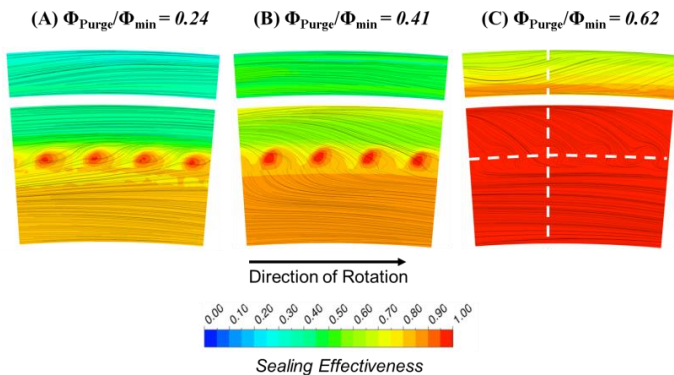


**Figure 11: Sealing Effectiveness with Cavity Streamlines on Axial Plane Bisecting the Rim Seal and Rim Cavity.**

In Figure 12, as  $\Phi_{\text{purge}}/\Phi_{\text{min}}$  is increased, the strength of the jet grows and is able to penetrate deeper axially across the rim cavity. This is evident in the angle of the stream lines relative to the rotating surface at the top of each illustration in Figure 12. The rotation of disk surface sets up a swirling flow field which the axial jets from the vane flow into. At high purge flow rates, the jets created by the purge air are able to penetrate all the way to the rotating wall, and the rim cavity becomes completely purged.

Sealing effectiveness in the near wall region between purge holes in Figure 12 is predicted to have a concentration gradient from nearly 0.5 at the wall to around 0.8 in the cavity free stream. This gradient is setup by flow above of the purge hole radius moving down the static wall, shown in the cross sectional images in Figure 10. Some of this flow moves

between purge holes, causing the predicted sealing effectiveness on the stator wall between holes. Figure 9 shows the modeling predicts lower sealing effectiveness than what is measured in the START rig by up to 0.2 effectiveness units. Since this is predicted to be a high gradient region, it's possible that the data at this location might be sensitive to the sampling flow rate, with higher sealing effectiveness air being drawn into the sampling tap from just outside the near wall region. This would cause the CFD prediction for sealing effectiveness to appear lower than experimental data. The rapid predicted increase in sealing effectiveness for  $\Phi_{\text{purge}}/\Phi_{\text{min}} > 0.62$  is caused by the reduction in this gradient, as the sealing effectiveness of the air OD of the purge hole is increased. It is also possible that the CFD model is not accurately predicting the mixing in this region and the gradient of sealing effectiveness is less severe in the rig.

The purge hole jets act to set up a buffer which separates the lower and upper part of the rim cavity. Since air is exiting the labyrinth seal in the lower part of the rim cavity, shown in Figure 1, flow is drawn across the jets, increasing the sealing effectiveness in the lower part of the cavity. In general sealing effectiveness in the lower rim cavity is above 0.80, observed with rig data at the purge holes and in the CFD.

The CFD prediction is consistent with the flow pattern behavior theorized by Clark et al. in [1], low axial momentum of the purge flow jets at low flow rates cause a rapid increase in sealing effectiveness at the static wall near the taps as the purge flow cannot penetrate far into the cavity and is drawn radially downwards by the overall cavity recirculation. At higher purge flow rates, the jets gain momentum and are able to penetrate deeper into the rim cavity, causing a steady, but slower increase in sealing effectiveness until the cavity is completely purged, as shown in Figure 9.

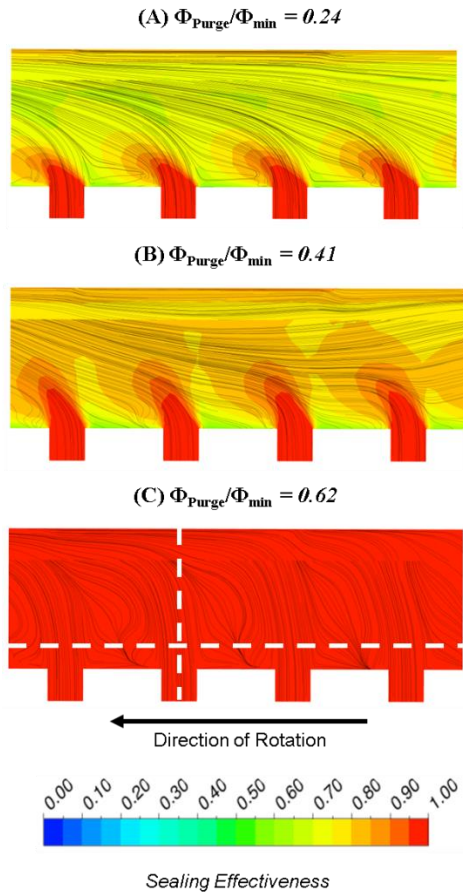


**Figure 12: Sealing Effectiveness with Cavity Streamlines at Vane Purge Hole Centerline Radius**

The radial placement of the vane purge holes will have a strong effect of the sealing effectiveness observed in the rim cavity. The modeling of the purge holes shows that they create a barrier to ingestion that is difficult to penetrate. It follows that more outboard holes would be beneficial in protecting the majority of the rim cavity from ingestion at the outer diameter. However, it should be noted that typical gas turbine rim cavities have a second source of purge air introduced at the seal between rotating and stationary structure at the inner diameter of the rim cavity. This purge source will influence the optimum positioning of static structure purge flow introduction locations. Modeling of turbine rim cavity designs with CFD has been shown through these studies have enough predictive capability to capture trends in sealing effectiveness, provided all leakage paths and geometry features are considered.

## CONCLUSION

A numerical model of the START rig rim cavity is developed and exercised for increasing vane purge flow rates. Results show trend-wise agreement between CFD predictions and measured sealing effectiveness at three locations on the static side of the rim cavity. The geometry and flows in the rim cavity are unique in the sense that they are representative of

realistic engine conditions. Because of the complexity of the geometry and leakage flows into and out of the rim cavity, sealing effectiveness trends at different locations in the rim cavity may not be well predicted using reduce order ingestion modeling. It has been demonstrated through this work that CFD modeling will capture trend-wise sealing effectiveness changes with increasing purge flow rates at specific locations in the rim cavity.

This study shows that geometry and rim cavity leakage flows have a strong influence the local sealing effectiveness. Because of these sensitives, one must exercise caution when developing CFD-based modeling, as differences in flows and geometry will influence predictions. The detailed modeling presented in this paper helps to explain trends observed in the experimental data set. Future design modifications, including the location of purge holes in rim cavities are envisioned to reducing ingestion and utilize purge air in a more efficient manner by directing it to areas of importance.

## REFERENCES

- [1] Clark, K., Barringer, M., Johnson, D., Thole, K. A., Grover, E., and Robak, C., 2018 “Effects of Purge Flow Configuration on Sealing Effectiveness in a Rotor-Stator Cavity” *Journal of Engineering for Gas Turbines and Power*, vol. 140(11), pp. 112502.
- [2] Owen, J.M., and Rogers, R.H., 1989. “Flow and Heat Transfer in Rotating-Disc Systems Volume 1 – Rotor-Stator Systems”, NASA STI/Recon Technical Report A 90
- [3] Sangan, C.M., Zhou, K., Owen, J.M, Pountney, O.J., Wilson, M., and Lock, G.D., 2013. “Experimental Measurements of Ingestion Through Turbine Rim Seals. Part 1: Externally-Induced Ingress”, *Journal of Turbo Machinery*, vol. 135 (2) p. 021012
- [4] Sangan, C.M., Zhou, K., Owen, J.M, Pountney, O.J., Wilson, M., and Lock, G.D., 2013. “Experimental Measurements of Ingestion Through Turbine Rim Seals. Part 2: Rotationally-Induced Ingress”, *Journal of Turbo Machinery*, vol. 135 (2) p. 021013
- [5] Beard, P.F., Chew, J., Gao, F., and Chana, K.S., 2017. “Unsteady Flow Phenomena in Turbine Rim Seals”, *Journal of Engineering for Gas Turbines and Power*, vol. 139 (3) p. 032501.
- [6] Julien, S., Lefrancois, J.,Dumas, G., Boutet-Blais, G., Lapointe S., Caron, J.F., and Marini, R., 2010. “Simulations of Flow Ingestion and Related Structures in a Turbine Disk Cavity” *ASME Turbo Expo 2010: Power for Land, Sea, and Air*, Vol 4, Paper No. GT2010-22729, pp. 1071-1080.
- [7] Chew, J.W., Cao, C., Millington, P.R., and Hogg, S.I., 2004. “Interaction of Rim Seal and Annulus Flows in an Axial Flow

Turbine”, *Journal of Engineering for Gas Turbines and Power*, Vol. 126, pp 786-793

[8] Rabs, M., Benra, F.K., Dohmen, H.J., Schneider, O., 2009, “Investigation of Flow Instabilities Near the Rim Cavity of a 1.5 Stage Gas Turbine”, *ASME Turbo Expo 2009: Power for Land, Sea, and Air*, pp. 1263-1272.

[9] Johnson, B.V., Jakoby, R., Bohn, D.E., and Cunat, D., 2009. “A Method for Estimating the Influence of Time-Dependent Vane and Blade Pressure Fields on Turbine Rim Seal Ingestion”, *Journal of Turbo Machinery* 131, no. 2, p.021005

[10] Savov, S., Atkins, N.R., “A Rim Seal Ingress Model Based on Turbulent Transport”, *ASME Turbo Expo 2017: power for Land, Sea, and Air*, Vol. 5B: Heat Transfer, GT2017-63531

[11] Hills, N.J., Chew, J.W., and Turner A.B., 2001. “Computational and Mathematical Modeling of Turbine Rim Seal Ingestion”, *ASME Turbo Expo 2001: Power for Land, Sea, and Air*, Vol 3, Paper No. 2001-GT-0204

[12] Wang, C.Z., Johnson, B.V., Mathiyalagan, S.P., Glahn, J.A., and Cloud, D.F., 2012. “Rim Seal Ingestion in a Turbine Stage from 360-Degree Time-Dependent Numerical Simulations”, *Journal of Turbo Machinery* 136, no. 3, p.031007

[13] Mirzamoghadam, A.V., Kanjiyani, S., Riahi, A., Vishnumolakala, R., Gundeti, L., 2015. “Unsteady 360 Computational Fluid Dynamics Validation of a Turbine Stage Mainstream/Disk Cavity Interaction”, *Journal of Turbomachinery*, Vol. 137, p. 011008

[14] O’Mahoney, T., Hills N.J., Chew, and J.W., Scanlon, T. 2010. “Large-Eddy Simulation of Rim Seal Ingestion”, *ASME Turbo Expo 2010: Power for Land, Sea, and Air*, Vol 4, Paper No. GT2010-22962, pp 1155-1165.

[15] Barringer, M. D., Coward, A. C, Clark, K., Thole, K. A., Schmitz, J., Wagner, J., Alvin, M. A., Burke, P., and Dennis, R., 2014. “The Design of a Steady Aero Thermal Research Turbine (START) for Studying Secondary Flow Leakages and Airfoil Heat Transfer,” *International Gas Turbine and Aeroengine Congress and Exposition*, Dusseldorf, Germany, GT2014-25570.

[16] Vandoormaals, J.P., and Raithby, G.D., 1984. “Enhancements of the SIMPLE Method for Predicting Incompressible Fluid Flow”. *Numer. Heat Transfer*, 147-163

[17] Patankar, S.V., 1980. “Numerical Heat Transfer and Fluid Flow”. Hemisphere, Washington DC.